Double magnetic phase transition in $ND_4Fe(DPO_4)_2$ and $NH_4Fe(HPO_4)_2$

B. F. Alfonso,[1] C. Piqué,[1] C. Trobajo,[2] J. R. García,[2] E. Kampert,[3] U. Zeitler,[3] J. Rodríguez Fernández,[4] M. T. Fernández-Díaz,[5] and J. A. Blanco[6]

[1]*Departamento de Física, Universidad de Oviedo, E-33204 Gijón, Spain*

[2]*Departamento de Química Orgánica e Inorgánica, Universidad de Oviedo, E-33006 Oviedo, Spain*

[3]*Institute for Molecules and Materials, High Field Magnet Laboratory, Radboud University Nijmegen, Toernooiveld 7, 6525 ED Nijmegen, The Netherlands*

[4]*CITIMAC, Facultad de Ciencias, Universidad de Cantabria, E-39005 Santander, Spain*

[5]*Institute Laue-Langevin, BP 156X, F-38042 Grenoble, France*

[6]*Departamento de Física, Universidad de Oviedo, E-33007 Oviedo, Spain*

(Received 3 June 2010; revised manuscript received 14 September 2010; published 20 October 2010)

Combining neutron diffraction, magnetization measurements up to 330 kOe and specific-heat data, we have studied in detail both the crystal and magnetic structures of triclinic $ND_4Fe(DPO_4)_2$ and $NH_4Fe(HPO_4)_2$ compounds. The low symmetry of this structure gives rise to a complex pattern of competing superexchange interactions between the magnetic moments of two types of Fe^{3+} sites (with different site symmetry) that are responsible for the existence of two magnetic phase transitions. Below $T_C = 17.82 \pm 0.05$ K $ND_4Fe(DPO_4)_2$ orders ferrimagnetically with the magnetic moments lying in the crystallographic plane *ac*. As the temperature is lowered to $T_t = 3.52 \pm 0.05$ K the compound undergoes a magnetic phase transition to an equal moment antiphase structure characterized by the propagation vector close to $\vec{k}_{AF} \approx (1/16, 0, 1/16)$ and a magnetic moment for the Fe^{3+} ions of 4.8 μ_B at 1.89 K. In addition, a two-step metamagnetic process is observed in the magnetization measurements at 2 K, where the antiphase ordering is destroyed under a field of only 2 kOe and the compound recovers the high-temperature ferrimagnetic ordering at around 20 kOe. The stability of this ferrimagnetic phase under magnetic field is only broken when the strength of the field reaches values as large as 180 kOe, and the magnetic moments begin to rotate to reach the full-induced ferromagnetic structure. A mean-field model has been used to account for the magnetization process leading to an estimation of the molecular-field coefficient of −2.86 K and the value of the critical magnetic field of 535 kOe to attain the full-induced ferromagnetic phase.

DOI: 10.1103/PhysRevB.82.144431 PACS number(s): 75.50.Ee, 61.05.F−, 61.66.Fn, 75.30.Et

I. INTRODUCTION

In recent decades there has been tremendous growth in the area of open-framework inorganic materials, built of interconnected MO_6 octahedra (M is a transition metal) and PO_4 tetrahedra because of their interesting chemical and physical properties and potential applications.[1–4] Specifically, the great utility of inorganic porous materials is intimately correlated to their geometrical features: the presence of cavities make them appropriate, for example, for catalysis, ion exchange, selective sorption, molecular sieves, optical components, detergents, and fertilizers.[5,6] Materials with an open-framework structure are not only limited to zeolites and other related natural materials. Since the first microporous aluminophosphate,[7] other multifunctional porous materials have been synthesized combining hydrothermal synthesis with the presence of cationic organic templates in the middle of the reaction.[8–10] The incorporation of transition-metal ions enabled investigation on magnetic open-framework materials. The first open-framework compound with transition-metal phosphates was synthesized by Corbin *et al.*,[11] although the first detailed study of an extensive family of open-framework iron-based phosphates with notable magnetic properties was not reported before 1996.[12–15]

The potential applications that would emerge by combining the magnetic properties of the transition metals with the rich structural chemistry (one-dimensional chain structures,[16] two-dimensional sheet structures,[9] and three-dimensional open-framework structures[17]) and compositional diversity of phosphates add impetus for research in the area of transition-metal phosphates.[18,19] The complex structural chemistry of these materials offers large variations of magnetic ion sublattice, which can lead to unusual crystal structures[20] and original magnetic responses. In particular, iron phosphates may perhaps represent one of the most interesting types of open-framework compounds. One of the main reasons is that iron possesses the ability to adopt different oxidation numbers as well as different coordination geometries, besides the diversity of magnetic superexchange interactions.[21–23]

In these materials the superexchange interactions are very important in determining the type of magnetic ordering. In a recent paper[23] on the structural and magnetic phases of $Fe(ND_3)_2PO_4$ it became clear that the magnetic structure is noncollinear with an incommensurate propagation vector $\vec{k}_{in} = (1/2 - \tau, 0, \tau)$ with $\tau \sim 0.04$ in reciprocal lattice units (rlu's), and that the magnitude of the Fe^{3+} magnetic moments is close to $\mu_{Fe} = 4.5$ μ_B at 4.2 K, describing a spiral ordering. This is possible when the superexchange interactions (two iron ions coupled through phosphate groups) in $Fe(ND_3)_2PO_4$ are frustrated and are dominant over the single-ion anisotropy. When we have compounds of very low symmetry, where the magnetic ions are located at different local symmetries, unusual magnetic behaviors can be induced.

 ©2010 The American Physical Society

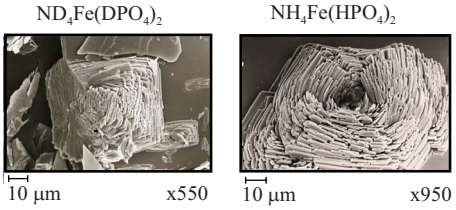

FIG. 1. (Color online) Scanning electron microscopy images showing the morphology of $ND_4Fe(DPO_4)_2$ and $NH_4Fe(HPO_4)_2$ samples.

In this paper we report on the magnetic properties of $ND_4Fe(DPO_4)_2$ and $NH_4Fe(HPO_4)_2$ studied by neutron powder diffraction, dc magnetization up to 330 kOe and specific heat. Neutron diffraction and specific heat clearly reveal the existence of two magnetic phase transitions; the magnetic structure of both have been determined. Using a mean-field model we have been able to account for the magnetization process observed at low temperatures. $NH_4Fe(HPO_4)_2$ was studied on a single crystal by x ray,[24] while the positions of the hydrogen atoms were determined by powder neutron diffraction,[20] and electron paramagnetic resonance experiments evidenced an isotropic signal characteristic of a high spin for the Fe^{3+} ions.[25]

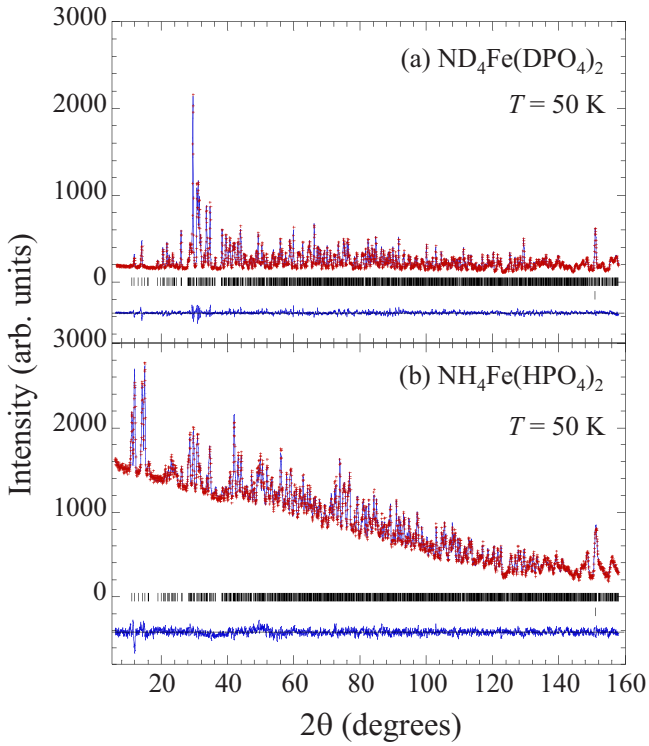

FIG. 2. (Color online) Observed (points), calculated (solid line) and difference (bottom) neutron-powder-diffraction (D2B) profiles of (a) $ND_4Fe(DPO_4)_2$ and (b) $NH_4Fe(HPO_4)_2$. Vertical marks correspond to the position of the allowed Bragg reflections associated with the crystal structure. In both patterns, the strong Bragg reflection near 155° is due to aluminium from the cryostat. It is worth noting that the refinement of both patterns (see text) leads to the same crystal structure (see Tables I and II) for both compounds, the differences observed in the patterns are related to the unlike scattering length for deuterium and hydrogen. The high background in the $NH_4Fe(HPO_4)_2$ compound is due to the high incoherent scattering length of hydrogen.

TABLE I. Crystal data and structure refinements at 50 K on D2B.

	$ND_4Fe(DPO_4)_2$		$NH_4Fe(HPO_4)_2$
Empirical formula	$FeP_2O_8ND_6$		$FeP_2O_8NH_6$
Crystal system		Triclinic	
Space group		$P\bar{1}$ (No. 2)	
Z		1	
Radiation probe		Neutron	
λ (Å)		1.594	
a (Å)	8.83860(5)		8.83906(9)
b (Å)	9.73954(5)		9.74191(10)
c (Å)	9.21292(5)		9.21435(9)
α (deg)	117.8573(5)		117.8492(7)
β (deg)	133.6068(4)		133.5947(6)
γ (deg)	80.6736(5)		80.6970(8)
V (Å^3)	491.557(5)		491.873(9)
2θ range (deg)	5–160		5–160
Step	0.05		0.05
Parameters	100		98
R_B (%)	3.39		5.85
R_F (%)	1.98		3.31
χ^2	2.43		2.03

II. EXPERIMENTAL

The preparation of the sample of both the deuterated and hydrogenated compounds has been described previously.[20] X-ray powder-diffraction measurements were carried out using a Seifert x-ray diffraction 3000 diffractometer, which confirmed the formation of a single phase in both samples. Rietveld fits to the x-ray powder data of both materials were performed using the FULLPROF Suite[26] to extract the cell parameters. A Quantum Design Physical Property Measurement System was used for magnetization and specific-heat measurements between 1.8 and 300 K under magnetic fields up to 90 kOe. Further magnetization measurements were carried out using a Bitter coil under magnetic fields up to 330 kOe at the High Field Magnet Laboratory (Nijmegen, NL) with a homemade vibrating-sample magnetometer.

Neutron-powder-diffraction measurements were performed on D2B (λ=1.594 Å) and D1B (λ=2.524 Å) diffractometers at the ILL facility. Data were collected at several selected temperatures (on D2B at 50, 12, and 2 K for the deuterated and hydrogenated compounds and on D1B every 1 K below 30 K only for the deuterated compound). The data were normalized to the incident-beam intensity and corrected for detector efficiency. Rietveld refinements of the crystal and magnetic structures were also carried out using the FULLPROF program.

TABLE II. Final fractional atomic positions and isotropic displacement parameters (Å^2) for $ND_4Fe(DPO_4)_2$ and $NH_4Fe(HPO_4)_2$ at 50 K on D2B.

	$ND_4Fe(DPO_4)_2$				$NH_4Fe(HPO_4)_2$			
Atom	*x*	*y*	*z*	*B*	*x*	*y*	*z*	*B*
Fe1	0.50000	0.50000	0.00000	0.55(2)	0.50000	0.50000	0.00000	0.03(1)
Fe2	0.3701(5)	0.9501(4)	0.6534(5)	0.16(2)	0.3734(9)	0.9493(6)	0.6512(9)	0.17(8)
P1	0.8477(10)	0.7813(7)	0.1925(10)	0.28(2)	0.8420(14)	0.7797(11)	0.188(2)	0.23(8)
P2	0.2703(10)	0.7778(7)	0.8255(10)	0.28(2)	0.2697(14)	0.7790(11)	0.829(2)	0.23(8)
P3	0.4748(10)	0.7687(7)	0.3531(10)	0.28(2)	0.4789(15)	0.7705(10)	0.360(2)	0.23(8)
O1	0.5037(8)	0.7951(7)	0.5491(9)	0.43(2)	0.4976(13)	0.7972(11)	0.546(2)	0.31(3)
O2	0.9179(8)	0.1886(6)	0.6768(9)	0.43(2)	0.9160(13)	0.1928(9)	0.681(2)	0.31(3)
O3	0.3450(9)	0.9377(6)	0.0337(10)	0.43(2)	0.3389(14)	0.9396(9)	0.031(2)	0.31(3)
O4	0.6163(9)	0.9097(6)	0.4339(10)	0.43(2)	0.6215(13)	0.9077(9)	0.4419(14)	0.31(3)
O5	0.3460(9)	0.7868(6)	0.7217(9)	0.43(2)	0.3492(12)	0.7834(10)	0.7190(13)	0.31(3)
O6	0.7892(9)	0.6459(7)	0.2003(9)	0.43(2)	0.7882(13)	0.6455(10)	0.2022(14)	0.31(3)
O7	0.5312(9)	0.6131(6)	0.2698(10)	0.43(2)	0.5329(13)	0.6155(9)	0.2781(14)	0.31(3)
O8	0.7766(8)	0.9277(7)	0.2604(10)	0.43(2)	0.7759(12)	0.9280(10)	0.260(2)	0.31(3)
O9	0.6628(8)	0.3582(6)	0.1209(9)	0.43(2)	0.6695(13)	0.3547(9)	0.1219(13)	0.31(3)
O10	0.2709(9)	0.2860(6)	0.0683(9)	0.43(2)	0.2686(13)	0.2899(9)	0.0729(13)	0.31(3)
O11	0.9864(9)	0.2597(6)	0.3588(9)	0.43(2)	0.9789(13)	0.2591(9)	0.3549(14)	0.31(3)
O12	0.7674(9)	0.2516(7)	0.8548(9)	0.43(2)	0.7687(12)	0.2470(9)	0.8501(13)	0.31(3)
N1	0.00000	0.00000	0.00000	0.94(2)	0.00000	0.00000	0.00000	0.84(8)
N2	0.1828(6)	0.4680(4)	0.3487(6)	0.94(2)	0.1825(10)	0.4684(7)	0.3469(10)	0.84(8)
D/H1	0.4116(10)	0.2577(7)	0.1537(11)	1.74(2)	0.417(3)	0.252(2)	0.151(3)	1.57(9)
D/H2	0.8426(10)	0.2317(7)	0.8039(11)	1.74(2)	0.858(3)	0.228(2)	0.801(3)	1.57(9)
D/H3	0.2255(10)	0.4151(8)	0.2557(11)	1.74(2)	0.237(3)	0.418(2)	0.267(3)	1.57(9)
D/H4	0.2326(9)	0.5919(7)	0.4364(10)	1.74(2)	0.225(2)	0.586(2)	0.435(2)	1.57(9)
D/H5	0.9824(10)	0.5653(7)	0.7645(10)	1.74(2)	0.983(3)	0.558(2)	0.760(3)	1.57(9)
D/H6	0.0657(10)	0.2933(7)	0.5168(11)	1.74(2)	0.073(2)	0.289(2)	0.520(3)	1.57(9)
D/H7	0.2588(9)	0.4311(7)	0.4691(10)	1.74(2)	0.261(2)	0.442(2)	0.484(3)	1.57(9)
D/H8	0.108(2)	0.9706(14)	0.998(2)	1.74(2)	0.135(5)	0.987(4)	1.049(5)	1.57(9)
D/H9	0.872(2)	0.9013(14)	0.095(2)	1.74(2)	0.871(5)	0.914(4)	0.095(6)	1.57(9)
D/H10	0.070(2)	0.0451(15)	0.183(2)	1.74(2)	0.086(5)	0.065(4)	0.191(5)	1.57(9)
D/H11	0.077(2)	0.9170(15)	0.040(2)	1.74(2)	0.069(5)	0.915(4)	0.030(5)	1.57(9)

III. RESULTS AND DISCUSSION

Both $ND_4Fe(DPO_4)_2$ and $NH_4Fe(HPO_4)_2$ crystallize with a needlelike structures (see Fig. 1). Due to the fibrous habit of these two materials,[27] their morphology is quite similar and consists of prisms whose base varies in size (1–5 μm).

Figure 2 shows the neutron-powder-diffraction patterns collected at 50 K on D2B for both $ND_4Fe(DPO_4)_2$ and $NH_4Fe(HPO_4)_2$. The two patterns can be indexed with a nonconventional triclinic $I\bar{1}$ space group[24] or with a reduced primitive unit cell using a triclinic $P\bar{1}$ space group[20] or, as in this work, with an alternative primitive unit cell $P\bar{1}$ that simplify the description of the magnetic structure of both $ND_4Fe(DPO_4)_2$ and $NH_4Fe(HPO_4)_2$ (see below). Both crystal structures were refined by the Rietveld method starting with atomic positions from the available x-ray powder and single-crystal data. Final cell parameters and coordinates including deuterium-/hydrogen-atom positions and isotropic displacement parameters are given in Tables I and II. It is worth noting that the primitive unit cell of $ND_4Fe(DPO_4)_2$ contains three Fe^{3+} ions on two different crystallographic sites with different local symmetry: one Fe1 located at the spatial inversion center and two Fe2 ions located on a site with only the identity symmetry.

A. Magnetic susceptibility

The temperature dependence of the molar magnetic susceptibility has been investigated. The magnetic measurements of both samples are identical within experimental uncertainty; for this reason, we show only those of $ND_4Fe(DPO_4)_2$. The field cooling and subsequently field-heating susceptibility data of $ND_4Fe(DPO_4)_2$ obtained under an applied magnetic field of 1 kOe are represented in Fig. 3.

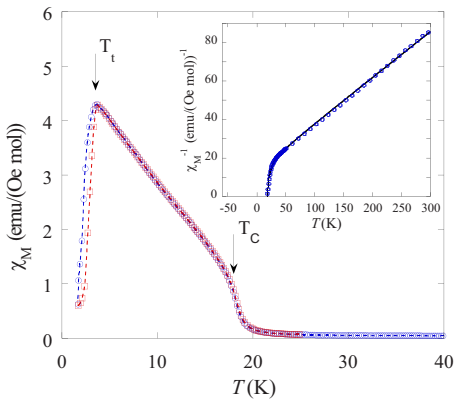

FIG. 3. (Color online) Temperature dependence of the molar magnetic susceptibility, χ_M, for $ND_4Fe(DPO_4)_2$ measured under a magnetic field of 1 kOe. The field-cooling (heating) data are open circle (square) points. The dashed lines are guides for the eyes. The inset shows a modified Curie-Weiss fit to the inverse molar magnetic susceptibility, χ_M^{-1}, according to Eq. (1) (see text).

A ferromagnetic (FM) [or ferrimagnetic (FI)] transition is observed as the magnetization $M(T)$ increases steadily below $T_C=18$ K while an antiferromagnetic (AF) ordering takes place below $T_t=3.5$ K owing to the sudden decreases found in $M(T)$. There is a small amount of thermal hysteresis between the field-cooling and field-heating susceptibility in the vicinity of the AF transition. The width of this hysteresis near T_t amounts to about 1 K. This irreversibility seems to be related to the magnetic domain pinning. The paramagnetic susceptibility follows a Curie-Weiss law in the temperature range of 300–50 K, but on approaching T_C, the susceptibility deviates from the Curie-Weiss law like a ferrimagnet (see inset in Fig. 3). The inverse molar magnetic susceptibility was fitted to the well-known Néel expression for a ferrimagnet

$$\chi^{-1} = (T-\Theta_P)/C - \gamma/(T-\Theta). \quad (1)$$

The refinement of Eq. (1) to the experimental data allows us to obtain the values for the paramagnetic Curie temperature Θ_P, the Curie constant C (from which the effective paramagnetic moment, μ_{eff}, can be determined), and the γ and Θ parameters. The best fit leads (see inset of Fig. 3) to the values of $\Theta_P=-61.5\pm0.5$ K, $\mu_{eff}=5.80$ μ_B, $\gamma=57\pm2$ emu^{-1} Oe mol K, and $\Theta=15.2\pm0.1$ K. The value of the μ_{eff} is slightly smaller than the theoretical effective paramagnetic moment for a highly isotropic Fe^{3+} ion ($L=0$, $S=5/2$, and $\mu_{eff}=5.92$ μ_B). Θ_P represents the sum of all the superexchange interactions, a negative value reveals that antiferromagnetic interactions are dominant in this compound. The relative high value of $|\Theta_p|/T_C\sim4$ is consistent with the presence of magnetic frustration. In addition, the fact that the fit to the paramagnetic susceptibility departs from the Curie-Weiss behavior below 50 K in $ND_4Fe(DPO_4)_2$ (see Fig. 3), as well as the existence of a subsidiary maximum near 25 K found in the specific-heat data (see below in Fig. 7) seems to suggest the existence of short-range magnetic correlations above T_C.

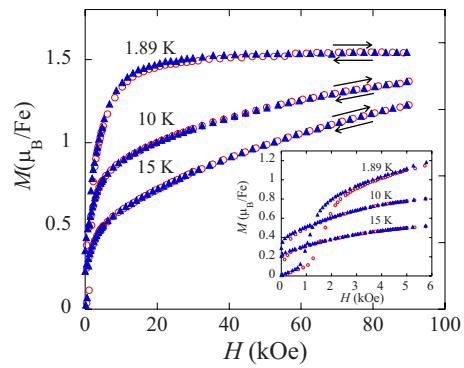

FIG. 4. (Color online) Magnetization isotherms with magnetic field increasing (open circles) or decreasing (solid triangles) for $ND_4Fe(DPO_4)_2$ measured up to a field of 90 kOe at selected temperatures 1.89, 10, and 15 K. The inset shows the detail of the low-field magnetization process.

B. Magnetization

The magnetization of $ND_4Fe(DPO_4)_2$ was first measured as a function of the field up to 90 kOe at several temperatures (see Fig. 4). The saturation magnetization $\mu_{Fe}=1.5$ μ_B/Fe at 1.89 K under 90 kOe is slightly lower than one third of the theoretical saturation moment expected for an $Fe^{3+}(3d^5)$ free magnetic moment ($\mu=2S$ $\mu_B=5$ μ_B). This important reduction may be attributed to the existence of two "up" an one "down" magnetic moments, following the arrangement ↑↓↑ (see below). While the magnetization isotherms measured at 10 and 15 K show a FI behavior, the isotherm measured at 1.89 K evidences the existence of a hysteretic metamagnetic process characterized by a critical magnetic field of 1.73 kOe, for increasing fields (see inset of Fig. 4). Note that after the metamagnetic process, the compound reaches a value of magnetization similar to that found at higher temperatures within the FI phase ($M\sim\frac{1}{3}M_{Fe^{3+}}$).

To get a better insight into the low-field magnetization curves, we carried out experiments at high magnetic fields up to 330 kOe. Several magnetization isotherms are represented in Fig. 5. The fact that the curves collected at 2 and 4.2 K are quite similar above 50 kOe indicates that the compound has the same ground state, as is also suggested by the H-T phase

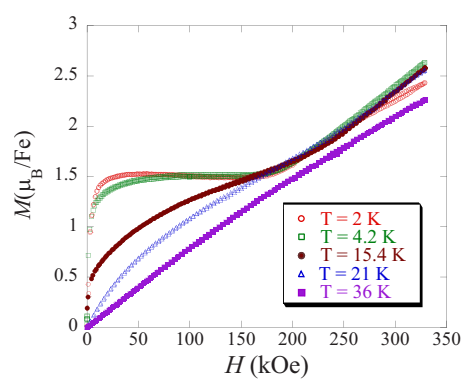

FIG. 5. (Color online) High-field magnetization measurements up to 330 kOe at selected temperatures on $ND_4Fe(DPO_4)_2$.

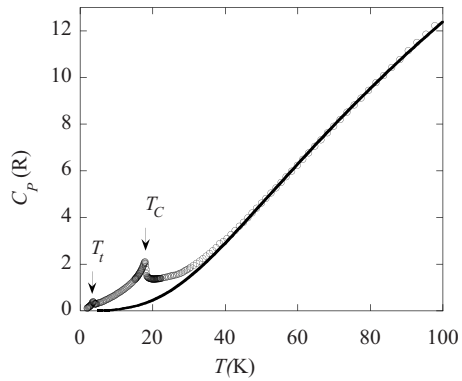

FIG. 6. The empty circles represent the heat-capacity experimental data of $ND_4Fe(DPO_4)_2$. T_t is the critical temperature of the AF phase while T_C is the Curie temperature for the ferrimagnetic ordering of the Fe^{3+} magnetic moments. The lattice contribution is represented by the solid line (see text).

diagram (see Fig. 8). This means that the magnetic arrangement of Fe2-Fe1-Fe2 ions ↑↓↑ is quite stable.

C. Specific heat

The temperature dependence of the specific heat, C_p, for zero magnetic field is represented in Fig. 6. Two λ-type anomalies were found around $T_C = 17.82 \pm 0.05$ K and $T_t = 3.52 \pm 0.05$ K, determined from the maximum of the anomaly, which are related to the ferrimagnetic and antiferromagnetic phase transitions, respectively. In order to extract the magnetic heat capacity, the lattice contribution until 100 K was represented by two Debye functions (only two free fitting parameters): a nine-dimensional Debye function with Debye temperature $T_{D1} = 245$ K and a 12-dimensional Debye contribution of characteristic temperature $T_{D2} = 460$ K. These values were refined in order to reproduce the experimental specific heat in the nonanomalous region. The procedure is similar to that used in Ref. 23. The contributions of the internal vibrations of the DPO_4 and ND_4 ions in this temperature range are negligible. The calculated baseline is represented in Fig. 6 as a continuous line and, after subtracting it from the experimental points, the resulting magnetic contribution, C_{mag}, is obtained as shown in Fig. 7(a). Near 25 K there is evidence of a shoulder or unresolved subsidiary maximum; such a feature could be associated with the persistence above T_C of pronounced short-range order due to low-dimensionality effects, as pointed out by Goñi[25] from electron paramagnetic resonance experiments. The jump of C_{mag} at T_C, $\Delta C_{mag} = 1.8R$, is close to the expected one for equal moment (EM) magnetic structures, $\Delta C_{mag}^{\mathrm{EM}} = 2.36R$ for $S = \frac{5}{2}$ within the molecular field approximation.[28] The effect of the magnetic field on the specific heat [see Fig. 7(a)] for the two λ-type anomalies is quite different. For the anomaly observed at T_C the field shifts the curve toward high temperatures while at T_t it is being shifted toward low temperatures. This behavior is indicating the FI character of the former and the antiferromagnetic character of the second. The magnetic entropy variation $\Delta S = \int \frac{C_{mag}}{T} dT$ is depicted in Fig. 7(b). The maximum entropy value is $1.70R$

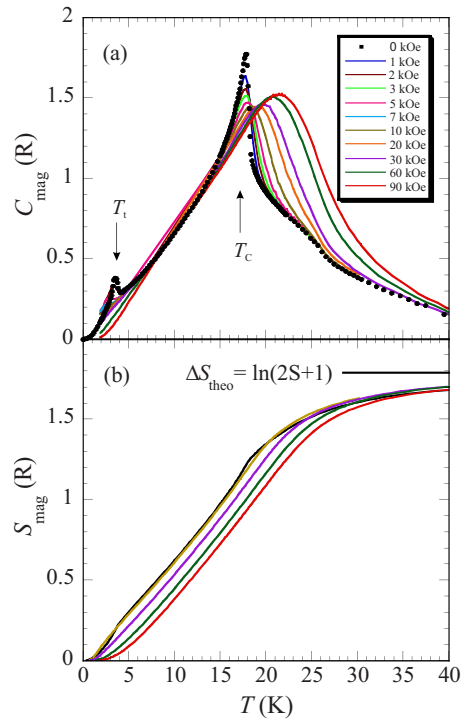

FIG. 7. (Color online) (a) Magnetic field dependence of specific heat for the $ND_4Fe(DPO_4)_2$ between 1.8 and 40 K. T_t is the critical temperature of the AF phase while T_C is the Curie temperature for the ferrimagnetic ordering of the Fe^{3+} magnetic moments. (b) Magnetic field dependence of the magnetic entropy, $\Delta S_{theo} = R \ln(2S+1) = 1.79R$ is the expected value for a $S = 5/2$ spin state.

at 40 K, in good agreement with the theoretical value: $1.79R$ for a compound with a magnetic moment of 5 μ_B (see below). Combining the information obtained from the magnetization curves together with the specific-heat data, we were able to plot the H-T phase diagram (see Fig. 8). The boundary between the AF and FI phases has been calculated by fitting the experimental points to the dependence $T_N(H) = T_N(0)\sqrt{1 - H/15}$.[29] It should be noted that the extrapolation value of H at $T_N = 0$ K, 15 kOe, is close to the value of the

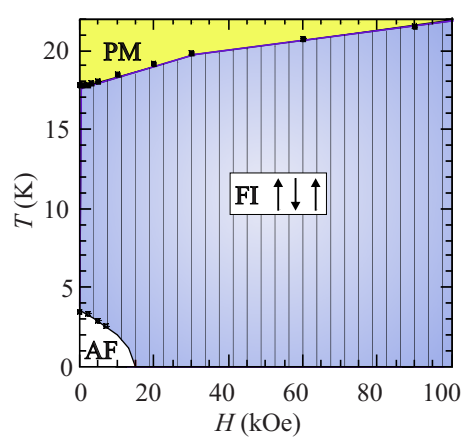

FIG. 8. (Color online) The H-T magnetic phase diagram of $ND_4Fe(DPO_4)_2$ based on the magnetization and specific-heat data. PM, FI, and AF are the paramagnetic, ferrimagnetic, and antiferromagnetic phases, respectively.

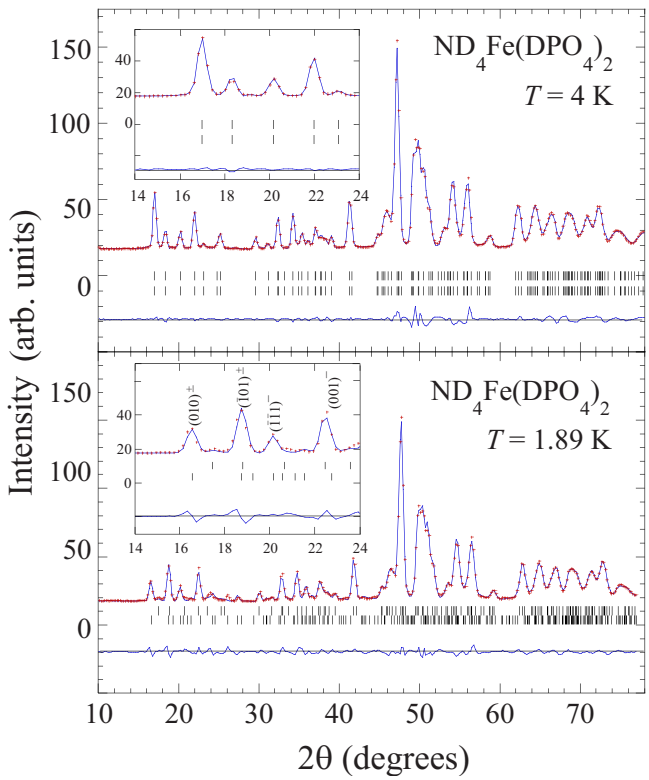

FIG. 9. (Color online) Powder neutron-diffraction patterns for $ND_4Fe(DPO_4)_2$ collected on (D1B). Observed (points) and calculated (solid line) values at 4 and 1.89 K. Bragg reflection positions are represented by vertical bars. The first (second) row of Bragg diffraction reflections corresponds to the nuclear (magnetic) peaks. The observed-calculated difference is depicted at the bottom of each pattern. In the pattern measured at 1.89 K within the AF phase the notation $(hkl)^{\pm}$ corresponds to magnetic reflections of type $(h+k_x,k,l+k_z)$ with $k_x=1/16$ and $k_z=1/16$ (see text).

field needed to saturate the magnetization at 1.89 K (see Fig. 4). The microscopic details of the different magnetic structures of $ND_4Fe(DPO_4)_2$ will be fully understood only after the neutron-scattering experiments (see below). Note the major stability of the FI phase within the *H-T* phase diagram.

D. Magnetic structures

Low-temperature D1B diffraction patterns were collected at several selected temperatures every 1 K below 30 K for deuterated compound. Figure 9 shows the D1B diffraction patterns at 4 and 1.89 K, below the first and second magnetic phase transition, respectively. We have also collected patterns on the D2B diffractometer measured at 12 and 2 K for both $ND_4Fe(DPO_4)_2$ and $NH_4Fe(HPO_4)_2$ compounds (Fig. 10). The refinement of these powder-diffraction patterns leads to conclude that within the experimental uncertainty the magnetic structures of both $ND_4Fe(DPO_4)_2$ and $NH_4Fe(HPO_4)_2$ compounds are the same. These results confirm the main issues obtained from the experiment carried out on D1B in $ND_4Fe(DPO_4)_2$ (see Table III). The analysis presented below is devoted to the D1B diffraction patterns, which are more appropriate for magnetic structure determination. The first patterns collected at 4 K (see Fig. 9) do not show any extra peaks different to those found at 50 K, thus indicating the FI character of the magnetic structure. Accordingly, all the magnetics peaks can be indexed with a propagation vector $\vec{k}=(0,0,0)$ referring to the 50 K crystallographic unit cell, indicating that the magnetic and nuclear unit cells are the same. Seeing as there are two types of Fe^{3+} ions, Fe1 and Fe2, located at very low local symmetry sites, Bertaut's microscopic theory is not very helpful when searching for the possible magnetic modes. Instead, Monte Carlo analysis was found to be very practical for determining that the actual directions of the magnetic moments of the two Fe1 and Fe2 sublattices are antiparallel, describing a FI ordering in accordance with Fig. 11. Other simpler magnetic

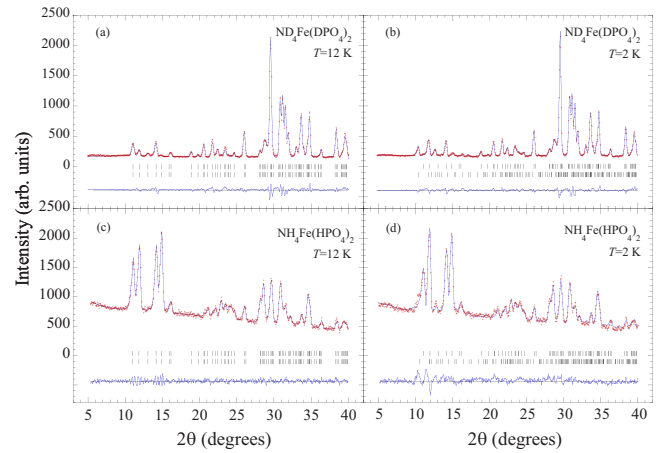

FIG. 10. (Color online) Observed (points) and calculated (solid line) powder-neutron-diffraction patterns collected on D2B for $ND_4Fe(DPO_4)_2$ (a) at 12 K, (b) at 2 K and for $NH_4Fe(HPO_4)_2$ (c) at 12 K, (d) at 2 K. Bragg reflection positions are represented by vertical bars. The first (second) row of Bragg diffraction reflections corresponds to the nuclear (magnetic) peaks. The observed-calculated difference is depicted at the bottom of each pattern. Within the experimental uncertainty the refinement of the magnetic diffraction patterns leads to propose the same magnetic structure for $ND_4Fe(DPO_4)_2$ and $NH_4Fe(HPO_4)_2$ samples (see text and Table III).

TABLE III. Comparison for the magnetic moments (μ_B) of the Fe(III) ions determined from powder neutron diffraction collected at 12 and 2 K (D2B) on both $ND_4Fe(DPO_4)_2$ and $NH_4Fe(HPO_4)_2$ compounds, and at 11, 4, and 1.89 K (D1B) on $ND_4Fe(DPO_4)_2$, and the corresponding R_B in %.

		T (K)	μ (μ_B)	R_B (%)
$ND_4Fe(DPO_4)_2$	D2B	12	3.1(2)	5.0
		2	4.8(2)	8.8
	D1B	11	3.4(2)	5.4
		4	4.2(2)	5.0
		1.89	4.8(1)	11.0
$NH_4Fe(HPO_4)_2$	D2B	12	3.2(3)	15.0
		2	4.6(3)	10.8

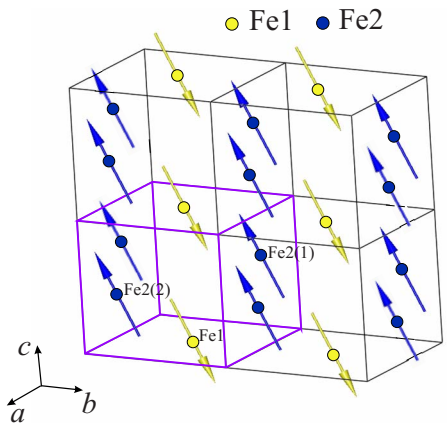

FIG. 11. (Color online) Representation of the magnetic moments of Fe1 and Fe2 ions within a unit cell for the ferrimagnetic ordering (see text).

arrangements such as considering all the Fe1 and Fe2 magnetic moments parallel with a collinear ferromagnetic ordering (or some of them zero) result on bad Bragg-reliability factors ($R_B > 30\%$). Rietveld refinement leads to a best solution for the magnetic structure of both the hydrogenated and deuterated materials with the magnetic moments in the *ac* plane. The agreement between the observed and calculated diffraction patterns for each possible magnetic structure were tested. The final refinement ($R_{mag} \sim 5\%$) leads to the following constraints and components for the magnetic moments along the crystallographic directions of the primitive unit cell (a,b,c): $\mu_{\mathrm{Fe}_{1a}} = -3.77\ \mu_B$, $\mu_{\mathrm{Fe}_{1b}} = 0\ \mu_B$, and $\mu_{\mathrm{Fe}_{1c}} = -5.84\ \mu_B$; $\vec{\mu}_{\mathrm{Fe1}} = -\vec{\mu}_{\mathrm{Fe2}}$, $\vec{\mu}_{\mathrm{Fe2(1)}} = \vec{\mu}_{\mathrm{Fe2(2)}}$, the total magnetic moment of all the Fe^{3+} ions being of magnitude $4.2 \pm 0.2\ \mu_B$. On the other hand, the temperature dependence of the modulus of the Fe magnetic moment, obtained from the refinement of the diffraction patterns collected between 3.8 and 25 K in the FI phase, is depicted in Fig. 12, where it is compared with the calculated dependence obtained from the Brillouin function for $S = \frac{5}{2}$. The agreement between the two variations is quite good, indicating that the superexchange interactions in this material are almost isotropic in character.

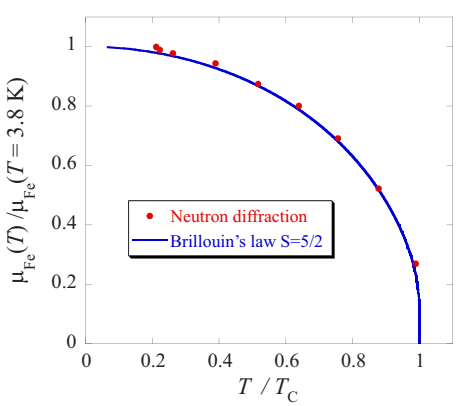

FIG. 12. (Color online) Temperature dependence of the Fe relative magnetic moment, μ_{Fe}, $\mu_{\mathrm{Fe}}(T)/\mu_{\mathrm{Fe}}(T=3.8\ \mathrm{K})$ obtained from neutron-diffraction data experiments on D1B compared with the Brillouin function, $S=5/2$ (see text).

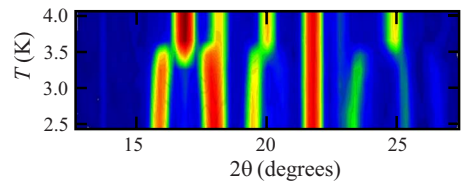

FIG. 13. (Color online) Intensity contour map of neutron-diffraction pattern of $ND_4Fe(DPO_4)_2$ collected at different temperatures from 2.5 K up to 4 K. Note the disappearance of Bragg magnetic peaks associated with the ferrimagnetic structure and the onset of the peaks related to the AF structure (see text). The magnetic peaks appearing below 3.5 K corresponding to the magnetic structure of the AF phase are those labeled in Fig. 9.

In contrast, the low-temperature diffraction pattern measured at 1.89 K on D1B, see Fig. 9, clearly presents extra magnetic peaks, the appearance of these AF peaks below 3.8 K in the low-temperature region is clearly seen across the magnetic phase transition, as shown in Fig. 13. The fact that the magnetic Bragg reflections have moderate intensities and the number of these reflections is not large makes it difficult to determine the magnetic structure from powder-diffraction data.[30,31] In fact, these extra magnetic peaks can be indexed with a propagation vector close to a long-period commensurate vector $\vec{k}_{\mathrm{AF}} \approx (1/16, 0, 1/16)$. The best refinement ($R_{mag} = 11\%$) corresponds to an antiphase magnetic structure formed from the same unit of the ferrimagnetic ordering found between 3.5 and 17.8 K in accordance with Fig. 14. The magnetic moments are arranged in $\uparrow\downarrow\uparrow$ blocks as is depicted in the aforementioned figure, where the magnetic periodicity is repeated after 16 crystallographic unit cells along the *a* and *c* directions. From the diffraction data collected at 1.89 K, the Fourier components of the magnetic moment for the principal harmonic is found to be $6.10 \pm 0.10\ \mu_B$, although no traces were detected for the other high-order harmonics. However, the Kramers character of the Fe^{3+} ion will, at low temperature, imply (due to entropy effects associated with the modulation of the magnetic-moment amplitude) having a spin system with a squaring up with all the high harmonics included, as depicted in Fig. 14. Accordingly, the experimental Fourier magnetic moment for the principal harmonic $M_{\vec{k}} = 6.10 \simeq 4/\pi \times 4.8\ \mu_B$ which is compatible with having an equal moment magnetic structure of 4.8 μ_B for the Fe^{3+} ions in the lattice. In this particular

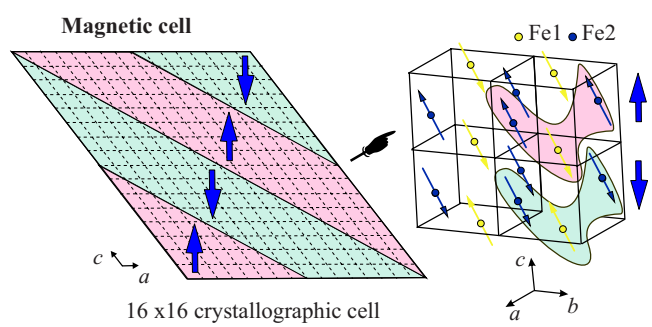

FIG. 14. (Color online) Schematic representation of the antiferromagnetic antiphase magnetic structure of $ND_4Fe(DPO_4)_2$ obtained from neutron diffraction at 1.89 K (see text).

TABLE IV. Structural data for $ND_4Fe(DPO_4)_2$, including selected geometrical parameters: multiplicity: m, direct distance Fe-Fe′ (DD), and bond Fe-O, O-O′, and O′-Fe′ lengths, length of superexchange pathway Fe-Fe′ (SE), and angles Fe-O-P, O-P-O′, and P-O′-Fe′ related to the possible magnetic superexchange pathways (see text) at 4 K.

Superexchange pathways	m	Fe-Fe′, DD (Å)	Fe-O (Å)	O-O′ (Å)	O′-Fe′ (Å)	Fe-Fe′, SE (Å)	Fe-O-P (deg)	O-P-O′ (deg)	P-O′-Fe′ (deg)
Fe1-O6-P1-O8-Fe2 (010)	2	4.60	2.02	2.56	1.96	6.02	131.4	114.2	152.8
Fe1-O7-P3-O4-Fe2 (010)	2	4.60	2.02	2.48	1.95	6.01	130.3	109.0	145.4
Fe1-O9-P2-O3-Fe2 (010)	2	4.60	1.95	2.55	1.95	6.97	165.1	112.0	130.1
Fe1-O6-P1-O2-Fe2 (100)	2	6.09	2.02	2.52	2.04	7.13	131.4	110.2	138.5
Fe1-O9-P2-O5-Fe2 (00$\bar{1}$)	2	6.09	1.95	2.49	2.05	7.06	165.1	108.8	134.4
Fe1-O7-P3-O1-Fe2 (000)	2	6.33	2.02	2.48	2.08	7.12	130.3	110.6	123.6
Fe2-O3-P2-O5-Fe2 (011)	1	4.65	1.95	2.55	2.05	7.07	130.1	112.5	134.4
Fe2-O5-P2-O3-Fe2 (011)	1	4.65	2.05	2.55	1.95	6.94	134.4	112.5	130.1
Fe2-O1-P3-O4-Fe2 (010)	1	5.15	2.08	2.48	1.95	7.05	123.6	110.5	145.4
Fe2-O4-P3-O1-Fe2 (010)	1	5.15	1.95	2.48	2.08	7.05	145.4	110.5	123.6
Fe2-O2-P1-O8-Fe2 ($\bar{1}$10)	1	5.17	2.03	2.49	1.96	6.98	138.5	112.7	152.8
Fe2-O8-P1-O2-Fe2 ($\bar{1}$10)	1	5.17	1.96	2.49	2.04	6.99	152.8	112.7	138.5

case, the absence of the principal well-separated harmonic and the well-defined high-order harmonics is well understood because the Bragg diffraction reflections would be expected to be observed at very low Bragg angles, inside the central neutron beam on D1B and D2B diffractometers. The high-order harmonics related to other Bragg reflections appearing at high angles are masked by nuclear reflections. Further experiments with larger neutron wavelengths are needed to obtain information on the existence of higher-order harmonics.

E. Model

The superexchange coupling paths Fe-O-P-O′-Fe′ between iron cations and their next-nearest neighbors in the Fe-Fe atomic range below 7 Å are presented in Table IV. Analysis was performed using the SIMBO program. As we have already pointed out, it should be noted that $ND_4Fe(DPO_4)_2$ presents two crystallographic sites for the Fe^{3+} ions, Fe1 and Fe2, and that the unit cell has two Fe2 and one Fe1, the latter located at an inversion center. Thus, the multiplicity, m, for the pathways that involve Fe1 is 2.

The superexchange coupling paths Fe-O-P-O′-Fe′ exist between Fe1 and Fe2 and also between Fe2 and Fe2. Therefore, each Fe1 iron interacts with two next-nearest neighboring Fe2, each one through three different paths. The Fe2 cation interacts with one next-nearest neighboring Fe2 through two different paths (see Fig. 15). There is no Fe-O-P-O′-Fe′ superexchange pathways within the Fe1 sublattice. Besides the length of the Fe-Fe′ superexchange pathway, these magnetic couplings are characterized by both the O-P-O′, Fe-O-P angles and the Fe-O, O-O′ bond lengths. For this $ND_4Fe(DPO_4)_2$ compound, the O-P-O′ angles range between 109° and 114° (close to the tetrahedral angle 109.5°), and the Fe-O distances are approximately 2 Å (see Table IV). However, the value of the Fe-O-P angles (between 130° and 165°) cannot ensure the type of coupling, according to Goodenough-Kanamori-Anderson rules.[32–34] Nonetheless, the bigger Fe-O-P and P-O′-Fe′ angles in the Fe1-Fe2 pathways could point toward antiferromagnetic superexchange coupling and the more similar and smaller Fe-O-P and P-O′-Fe′ angles in the next-neighbor Fe2-Fe2 superexchange pathway could suggest a ferromagnetic coupling.

To explain the magnetization process of $ND_4Fe(DPO_4)_2$ we have adopted the following expression for the free energy in the mean-field approximation:

$$E = -2M_0H\cos\theta - M_0H\cos\varphi - 2\lambda M_0^2\cos(\theta+\varphi), \quad (2)$$

where H is the applied magnetic field, φ and θ are the angles of the Fe1 and Fe2 magnetic moments with the applied magnetic field (z-local axis), respectively, M_0 is the iron magnetic moment, and λ is the molecular field exchange parameter (see Fig. 16). The two first terms in Eq. (2) are the Fe2 and Fe1 Zeeman energies, respectively, while the last term

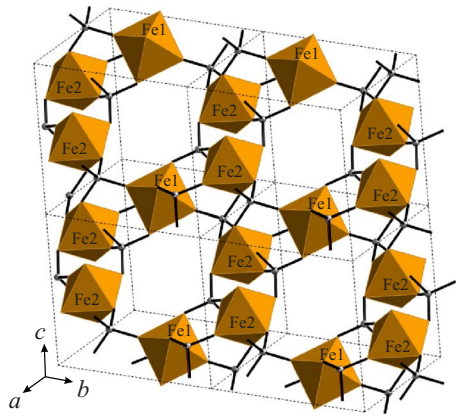

FIG. 15. (Color online) Polyhedral representation of the crystal structure of $ND_4Fe(DPO_4)_2$. The solid lines indicate the superexchange pathways between iron cations, the grey spheres are P atoms and the orange octahedra are FeO_6 units.

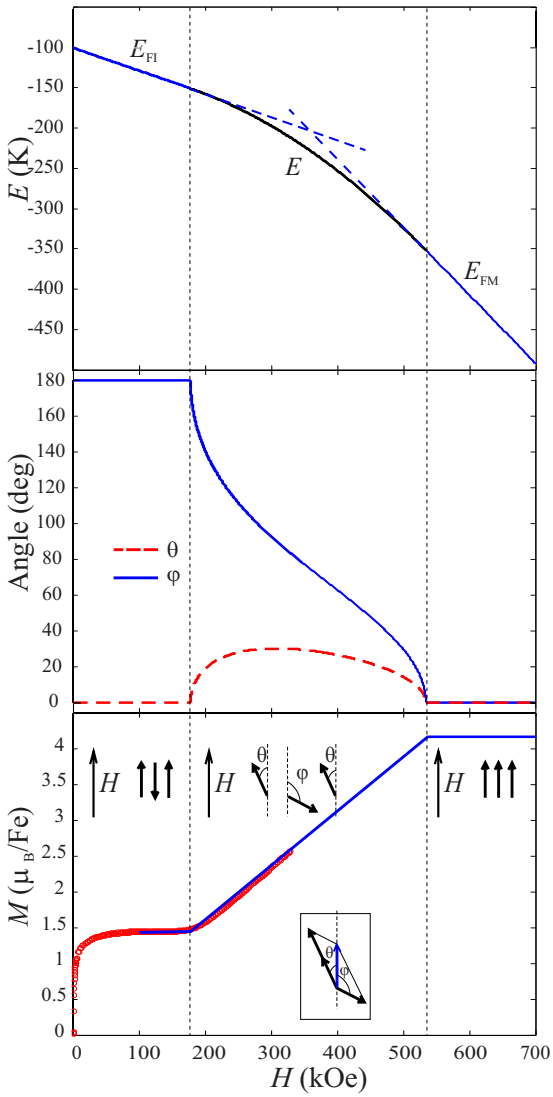

FIG. 16. (Color online) Calculated field dependence of the free energy of the initial (E_{FI}), intermediate (E), and final (E_{FM}) states, angles (θ and φ), and magnetization (M) together with the experimental magnetization curve at 4 K (○).

represents the exchange interactions between the Fe1 and Fe2 magnetic sublattices. We have made the assumptions that the anisotropy is negligible and that the biggest interaction is the one within the Fe2 sublattice.

The minimization of Eq. (2) with respect to θ and φ gives the equilibrium orientations of the iron magnetic moments for each magnetic field. The solutions are

$$\sin\theta = 0, \quad \sin\varphi = 0, \tag{3}$$

$$\cos\theta = \frac{h^2+3}{4h}, \quad \cos\varphi = \frac{h^2-3}{4h}, \tag{4}$$

where $h=(H\lambda)/M_0$. The solution will be valid if, and only if, $-1 \leq \cos\theta \leq 1$ and $-1 \leq \cos\varphi \leq 1$.

Thus, the total magnetization per Fe^{3+} under the applied magnetic field will be

$$M = 1/3M_0(2\cos\theta + \cos\varphi). \tag{5}$$

We refined the values of λ to account for the observed magnetization curve at 4 K. The best solution leads to the value $\lambda = -2.86$ K. The field dependence of the free energy corresponding to the initial, the intermediate, and the final states, the angles θ and φ, and the magnetization are represented in Fig. 16. The lowest energy will determine the ground state of the compound for each magnetic field. At zero field the most stable solution corresponds to $\theta=0$ and $\varphi=\pi$ and the arrangement ↑↓↑, as expected. This state is stable until reaching a critical field of around 180 kOe when the compound is able to overcome the negative superexchange interactions. The Fe1 and Fe2 magnetic moments tilt away from the axis, maintaining the total magnetization along the magnetic field, as the strength of the applied magnetic field increase. This makes that the θ angle first increases until 30° to decrease subsequently to zero. Above 535 kOe, the compound would attain the ferromagnetic arrangement ↑↑↑. Both the experimental and calculated magnetization are in very good agreement, indicating that the assumptions made in the model are meaningful.

It can be observed that slight geometrical differences in the parameters of the pathways (angles and interatomic distances) even lead to changes in sign for the superexchange interactions Fe-O-P-O′-Fe′ (ferro for Fe2-Fe2 and antiferro for Fe1-Fe2). The low symmetry of the crystal structure and the great number of superexchange pathways involved, which are susceptible to variations in temperature, are responsible for the low-temperature complex magnetic structure found in the $ND_4Fe(DPO_4)_2$.

IV. CONCLUSIONS

In summary, $ND_4Fe(DPO_4)_2$ which has two type of Fe^{3+} magnetic sites, presents two magnetic phase transitions below the ordering temperature $T_C = 17.82 \pm 0.05$ K. It first orders ferrimagnetically because the number of ions in the two different magnetic sublattices is different, and then it undergoes a magnetic phase transition to an antiphase magnetic structure below $T_t = 3.52 \pm 0.05$ K. We have shown that the metamagnetic process occurs in two steps in $ND_4Fe(DPO_4)_2$ at 2 K. First, a ferrimagnetic phase is reached around 20 kOe which is stable under a large range of magnetic applied fields, and only after 180 kOe does this magnetic-moment arrangement become unstable. Such behavior is quite well accounted for by a molecular field model that takes into account the exchange interactions between nearest neighbors in the lattice. Joint analysis of the magnetization measurements together with the neutron-diffraction experiments enabled us to determine the magnitude of the superexchange interaction between the Fe1 and Fe2 magnetic sublattices quantitatively (−2.86 K).

ACKNOWLEDGMENTS

This work has been carried out with the financial support of FEDER-MEC (Grants No. MAT2006-01997, No. MAT2008-06542-C04, and Factoría Española de Cristalización Consolider Ingenio 2010). Part of this work has been

supported by EuroMagNet under the EU under Contract No. 228043. We wish to thank J. Rodríguez-Carvajal for providing us with the SIMBO program and for useful discussions and suggestions. We also thank ILL and Spanish CRG-D1B for allocating neutron beam time. SCTs from the University of Oviedo are also gratefully acknowledged.

[1] A. K. Cheetham, G. Ferey, and T. Loiseau, Angew. Chem., Int. Ed. **38**, 3268 (1999).
[2] N. Rajic, J. Serb. Chem. Soc. **70**, 371 (2005).
[3] D. Maspoch, D. Ruiz-Molina, and J. Veciana, Chem. Soc. Rev. **36**, 770 (2007).
[4] R. Murugavel, A. Choudhury, M. G. Walawalkar, R. Pothiraja, and C. N. R. Rao, Chem. Rev. **108**, 3549 (2008).
[5] A. Corma, Curr. Opin. Solid State Mater. Sci. **2**, 63 (1997).
[6] A. Bhaumik, Proc.-Indian Acad. Sci., Chem. Sci. **114**, 451 (2002).
[7] S. T. Wilson, B. M. Lok, C. A. Messina, T. R. Cannan, and E. M. Flanigen, J. Am. Chem. Soc. **104**, 1146 (1982).
[8] J. R. D. DeBord, W. M. Reiff, R. C. Haushalter, and J. Zubieta, J. Solid State Chem. **125**, 186 (1996).
[9] Y. N. Song, P. Y. Zavalij, N. A. Chernova, and M. S. Whittingham, Chem. Mater. **15**, 4968 (2003).
[10] J. M. Rojo, J. L. Mesa, L. Lezama, J. L. Pizarro, M. I. Arriortua, J. Rodriguez Fernandez, G. E. Barberis, and T. Rojo, Phys. Rev. B **66**, 094406 (2002).
[11] D. R. Corbin, M. M. Eddy, J. F. Whitney, W. C. Fultz, A. K. Cheetham, and G. D. Stucky, Inorg. Chem. **25**, 2279 (1986).
[12] M. Cavellec, D. Riou, C. Ninclaus, J. M. Greneche, and G. Ferey, Zeolites **17**, 250 (1996).
[13] M. Cavellec, D. Riou, J. M. Greneche, and G. Ferey, J. Magn. Magn. Mater. **163**, 173 (1996).
[14] A. A. Belik, M. Azuma, A. Matsuo, M. H. Whangbo, H. J. Koo, J. Kikuchi, T. Kaji, S. Okubo, H. Ohta, K. Kindo, and M. Takano, Inorg. Chem. **44**, 6632 (2005).
[15] A. A. Belik, M. Azuma, A. Matsuo, T. Kaji, S. Okubo, H. Ohta, K. Kindo, and M. Takano, Phys. Rev. B **73**, 024429 (2006).
[16] S. Mandal, S. Natarajan, W. Klein, M. Panthöfer, and M. Jansen, J. Solid State Chem. **173**, 367 (2003).
[17] K.-H. Lii, Y.-F. Huang, V. Cima, C.-Y. Huang, H.-M. Lin, Y.-C. Jiang, F.-L. Liao, and S.-L. Wang, Chem. Mater. **10**, 2599 (1998).
[18] M. Riou-Cavellec, J. Greneche, and G. Ferey, J. Solid State Chem. **148**, 150 (1999).
[19] S. Natarajan and S. Mandal, Angew. Chem., Int. Ed. **47**, 4798 (2008).
[20] B. F. Alfonso, J. A. Blanco, M. T. Fernandez-Diaz, C. Trobajo, S. A. Khainakov, and J. R. Garcia, Dalton Trans. **39**, 1791 (2010).
[21] P. D. Battle, T. C. Gibb, G. Hu, D. C. Munro, and J. P. Attfield, J. Solid State Chem. **65**, 343 (1986).
[22] B. F. Alfonso, C. Trobajo, M. A. Salvado, P. Pertierra, S. Garcia-Granda, J. Rodriguez Fernandez, M. T. Fernandez-Diaz, J. A. Blanco, and J. R. Garcia, J. Phys.: Condens. Matter **20**, 104227 (2008).
[23] B. F. Alfonso, C. Trobajo, C. Pique, M. T. Fernandez-Diaz, J. Rodriguez Fernandez, M. A. Salvado, P. Pertierra, S. Garcia-Granda, J. R. Garcia, and J. A. Blanco, Acta Mater. **58**, 1741 (2010).
[24] O. V. Yakubovich, Kristallografiya **38**, 43 (1993).
[25] A. Goñi, L. Lezama, A. Espina, C. Trobajo, J. R. García, and T. Rojo, J. Mater. Chem. **11**, 2315 (2001).
[26] J. Rodríguez-Carvajal, Physica B **192**, 55 (1993).
[27] M. A. Salvadó, P. Pertierra, S. García-Granda, A. Espina, C. Trobajo, and J. R. García, Inorg. Chem. **38**, 5944 (1999).
[28] J. A. Blanco, D. Gignoux, P. Morin, and D. Schmitt, J. Magn. Magn. Mater. **90-91**, 166 (1990).
[29] R. A. Fisher, P. Radhakrishna, N. E. Phillips, J. V. Badding, and A. M. Stacy, Phys. Rev. B **52**, 13519 (1995).
[30] J. A. Blanco, J. I. Espeso, J. Garcia Soldevilla, J. C. Gomez Sal, M. R. Ibarra, C. Marquina, and H. E. Fischer, Phys. Rev. B **59**, 512 (1999).
[31] J. I. Espeso, J. Garcia Soldevillla, J. A. Blanco, J. Rodriguez Fernandez, J. C. Gomez Sal, and M. T. Fernandez-Diaz, Eur. Phys. J. B **18**, 625 (2000).
[32] J. B. Goodenough, *Magnetism and Chemical Bond* (International, New York, 1963).
[33] J. J. Kanamori, J. Appl. Phys. **31**, S14 (1960).
[34] P. W. Anderson, *Magnetism a Treatise on Modern Theory and Materials* (Academic Press, New York, 1963), Vol. I.